www.pnas.org

Supplementary Information for

Large and projected strengthening moisture limitation on end-of-season photosynthesis

Yao Zhang, Nicholas Parazoo, A. Park Williams, Sha Zhou, Pierre Gentine

*Correspondence to: Yao Zhang and Pierre Gentine
Emails: yaozhang@lbl.gov; pg2328@columbia.edu

This PDF file includes:

Supplementary text S1 to S5
Figures S1 to S19
Tables S1 to S3
SI References

Supplementary Information Text

Text S1. CSIF dataset

CSIF dataset is trained on 2-years of co-location OCO-2 SIF and MODIS MCD43 BRDF adjusted reflectance. The performance comparison between this dataset and OCO-2 or other SIF retrievals are compared in details in a previous study (1). Here we would like to further discuss the advantage and potential caveats of this dataset.

Comparison with other GPP dataset

Comparing with other machine learning algorithms that directly trained on GPP dataset (e.g., FLUXCOM (2)), the CSIF dataset uses much more training samples (>1,800,000), and these samples suffers less from the spatial representative issues compared to those from flux tower sites which are concentrated in mid-latitudes. But this does not necessarily mean that CSIF has a better overall performance than FLUXCOM in representing GPP due to the uncertainties in SIF-GPP relationship. Compared to other light use efficiency based GPP models, we do not impose any fixed relationship between surface reflectance and SIF, making the NN more flexible in capturing the vegetation signal. Although the GPP-SIF relationship may change for different biome types (3), this would not affect the EOP retrieval since the seasonal curve were normalized for each pixel before phenology retrieval.

Effectiveness to estimate SIF from reflectance

Previous studies have demonstrated that SIF signals observed by satellite can be decomposed into absorbed PAR by chlorophyll ($APAR_{chl}$), fluorescence efficiency, and the escape factor (4, 5). The fluorescence efficiency describes the dynamic partitioning of energy into fluorescence and is tightly linked to the photochemical efficiency. The escape factor describes the scattering and reabsorption of SIF emission by other leaves with in the canopy. Among these, changes in both $fPAR_{chl}$, and escape factor dominate the seasonal dynamic of SIF signal in most ecosystems and can be directly link to the canopy structure and leaf biochemistry (6, 7). Therefore, SIF can be potentially estimated from canopy reflectance (8).

Several recent studies have demonstrated the use of exclusive reflectance information to estimate ecosystem scale GPP and also showed very strong correlation with satellite retrieved SIF signal (9, 10). This can be explained by the fact that canopy structure (especially leaf angle distribution) strongly modulates the reflectance in near infrared (NIR) band, and can also be linked to the scattering of the SIF signal as well as the total photosynthesis of the canopy (8). In several ecosystem types (e.g., cropland), this correlation is even stronger than the correlation between GPP and SIF measurement at canopy level, possibly due to less noise in reflectance measurements (7). In addition, this canopy structural changes can also contain plant physiological signal. For example, when drought stress becomes a limiting factor to photosynthesis, leaf angle distribution would also change to intercept less energy as self-protection (11). This process would greatly affect the NIR and operate at a much faster pace than the change of leaf color that can be captured by NDVI and other vegetation indices. The change in NIR can also be an indicator of changes in canopy scattering of SIF signals observed by satellite. Recent studies also demonstrated the importance of leaf scattering in driving the satellite or canopy level SIF signal and GPP variations (12). Therefore, using exclusively reflectance dataset, we can still get much of the information (PAR absorption by chlorophyll, canopy scattering, and potentially stress on in fluorescence yield) in the SIF signal, as well as ecosystem photosynthesis.

Although only two years (2015-2016) of training data were used, our NN showed very good performance in validation using two other years (2014, 2017) (R^2=0.796 RMSE=0.182 for training, and R^2=0.786 RMSE=0.177 for validation). This suggests the model may capture the generalized SIF-reflectance relationship and this relationship can be used to predict SIF for other years.

Potential caveats

For some specific ecosystems (evergreen needleleaf forest), the sustained temperature stress on photosynthesis during winter time may not be well captured by this approach. In these ecosystems, the canopy structure changes are relatively small and fluorescence yield changes contributed most to the seasonal changes of SIF and GPP and cannot be effectively captured by the broad band remote sensing reflectance (13). However, this may have limited effect on phenology derivation since the CSIF time series is normalized first. As shown in SI Appendix Fig. S2C, the interannual variability of CSIF derived EOP still have strong correlation with EOP estimated from EC towers, even for the evergreen needleleaf forest and mixed forest sites. The magnitude of interannual variability for these biome type can be underestimated, but since the metric we used to quantify temperature and water limitation on EOP is based on correlation coefficient, this underestimation should not affect our results.

It should also be noted that all these remote sensing-based indicators (including SIF) do not change at the same magnitude as GPP in response to droughts, potentially underestimating the drought effect, especially for forest ecosystems (14). However, since we do not focus on the absolute values of EOP sensitivity to precipitation or temperature, but rather on the correlation coefficients between them, this underestimation of drought impact should not affect our conclusion. Compared to deciduous forest, the CSIF decrease in needleleaf forest is smaller, but still larger than other VIs, demonstrating its superior skill. The comparison between pre- and within drought changes also demonstrate that CSIF can better capture the shifts from positive (or near neutral) to negative photosynthesis anomalies as droughts progress.

Text S2. Near-infrared reflectance of vegetation (NIR_V) dataset

In addition to the CSIF dataset, we also use NIR_V to further support our analysis. NIR_V measures the near-infrared reflectance from vegetation, which is suggested to be sensitive to canopy structural effect on photosynthesis (9). To be consistent with the dataset used to generate CSIF and other studies (9, 10), we use the daily Nadir BRDF adjusted reflectance (MCD43C4 V006) to calculate NIR_V, along with two standard vegetation indices, EVI and NDVI. The reflectance is first quality-checked; only pixels that meet three criteria are used: (1) less than 50% of snow cover, (2) more than 50% of valid fine resolution (500 m) data contribute to this 0.05 grid, and (3) less than 50% of the filled BRDF inversions. VIs are then calculated using the quality-checked reflectance and then aggregated to 4-day temporal and 0.5°×0.5° spatial resolution.

Since NIR_V and other VIs are very sensitive to atmospheric conditions and snow, special treatment is required to eliminate these contaminated values. We use air temperature either from EC site (for site-level comparison) or ERA5 reanalysis (for global analysis) data to identify the pixels that may potentially affected by snow (mean daily air temperature (Ta) below 5℃), and use a background VI value to replace these gaps for each pixel. The background VI value is determined as follows: using the VI values from multiple years, we find the minimum values (2% quantile) during the period that are not potentially affected by snow (Ta>5℃). This value is then used to fill the gaps during the non-growing season. Short gaps during the growing season caused by cloud are linearly gap-filled. This method better captures the seasonal magnitude of VI and can better retrieve phenology (15).

Text S3. Climate datasets

ERA-Interim

We used air temperature at 2 m (‘t2m’), total precipitation (‘tp’) and photosynthetically active radiation (‘par’) from the ERA-Interim dataset. The ERA-Interim reanalysis dataset is generated with a sequential data assimilation system, and provided a coherent record of atmospheric evolution constrained by various observations both from satellite and ground (16). These three variables have a daily temporal resolution and 0.5° spatial resolution.

MYD11A2

We used the land surface temperature (LST) from the MYD11C2 which has an overpass time of 13:30 and 01:30 local time. These two observations were used to represent the maximum and minimum daily LST. The MYD11C2 data are greatly affected by clouds and the observations were aggregated from 0.05° resolution to 0.5° resolution with only the highest-quality data. Although there is a difference between the air temperature and LST during clear-sky conditions, the average of daytime and nighttime LST can minimize this discrepancy (17).

GPCP

The global precipitation climatology project (GPCP) (18) provides global precipitation by integrating satellite data and gauge observations over land. We used the v1.3 1 degree daily (1DD) precipitation (19) and further spatially interpolated to 0.5º resolution. This dataset combines the threshold-matched precipitation index (TMPI) with locally set brightness temperature threshold and conditional rain rate between 40ºS to 40ºN, and a rescaled daily Television and infrared Observation Satellite Operation Vertical Sounder (TOVS) precipitation for higher latitude. This dataset is mostly observation-based and is independent from the reanalysis data.

BESS PAR

The BESS PAR dataset is generated from an atmospheric radiative transfer model coupled with a neural network using MODIS atmospheric dataset as input (20). This dataset has been validated against in situ observations and showed high accuracy. We used the daily 0.05º dataset and aggregated to 0.5º to match other datasets.

SMAP soil moisture

We used surface soil moisture retrievals from the SMAP L-band radiometer measurements (21). The inversion of the soil moisture is based on solving a radiative transfer model commonly known as τ–ω model, in which the measured brightness temperature (T_B) is a combination of soil temperature scattered by the opaque vegetation layer and vegetation temperature reflected and scattered by soil and vegetation. Either combining with ancillary information or using a multichannel approach, soil reflectivity can be estimated through τ–ω model. Surface soil moisture can be then estimated from soil reflectivity using the dielectric model and ancillary information on soil texture. Although the soil moisture retrieved at L-band (1.4 GHz) can only represent the upper 5 cm, the 6:00 AM overpass measurement may represent deeper soil moisture due to the hydraulic redistribution of the plant's roots. The satellite-based soil moisture estimates may have large uncertainty when the land is covered by snow/ice or dense vegetation (e.g., tropical rainforest) (22). However, we only focus on the late growing season and the tropical rainforests are eliminated from analysis due to the weak seasonality and high biomass that may affect the quality of the retrieval.

Text S4. FLUXNET data quality check

The following criteria were used to check the data quality for FLUXNET2015 i) For each site, the daily GPP estimates based on the nighttime partitioning method (23) and the corresponding net ecosystem exchange data quality ("NEE_VUT_REF_QC") were first aggregated to monthly values. Months with more than 50% of the un-gapfilled NEE observations were regarded as "valid months", and a mean seasonal cycle of GPP (GPP_{MSC}) was calculated using "valid months" from all years. The climatological average EOP month was first roughly determined as the month with GPP less than a threshold (minimum GPP + 30% seasonal amplitude). For each year, at least two out of three months before and during the climatological average EOP month should be "valid months". ii) For each year, at least half of the months during the photosynthetically active months (monthly average GPP>1 g C m^{-2} d^{-1}) should be "valid months". iii) After the data quality check, sites with more than 5 years of valid observations will be considered. iv) Sites strongly influenced by human management will not be used (cropland, pasture, etc.). v) Sites with small seasonality will not be used (minimum $\mathrm{GPP_{MSC}}$ > 0.3×maximum $\mathrm{GPP_{MSC}}$). 50 sites passed these criteria and were used for the analysis (SI Appendix, Table S2).

Text S5. Independent thresholds for water and temperature-limited regions separation

In addition to the SVM method used in the main text to separate the regions limited by temperature and precipitation, we also tested a threshold-based algorithm. This algorithm uses a combination of two thresholds for MAT and pre-EOP SM, respectively, to separate the temperature and precipitation limited regions. The L2 (mean squared error) loss function is written as:

$$\underset{\theta_{\mathrm{MAT}},\theta_{\mathrm{SM}}}{\operatorname{argmin}}\ L(\hat{y} = \mathrm{MAT} > \theta_{\mathrm{MAT}} | \mathrm{SM} < \theta_{\mathrm{SM}}, y)$$

where y and $\hat{y}$ are the observed and predicted classification, respectively. The two thresholds ($\theta_{\mathrm{MAT}}, \theta_{\mathrm{SM}}$) divide the MAT and pre-EOP SM into four regions, with the bottom right (high SM, low MAT) being limited by temperature, and other three being considered as precipitation limited. We used the "L-BGGS-B" method with the R base function "optim" for optimization. The optimization was bootstrapped 2000 times and the median values of the two thresholds were used to calculate the classification accuracy and kappa coefficient.

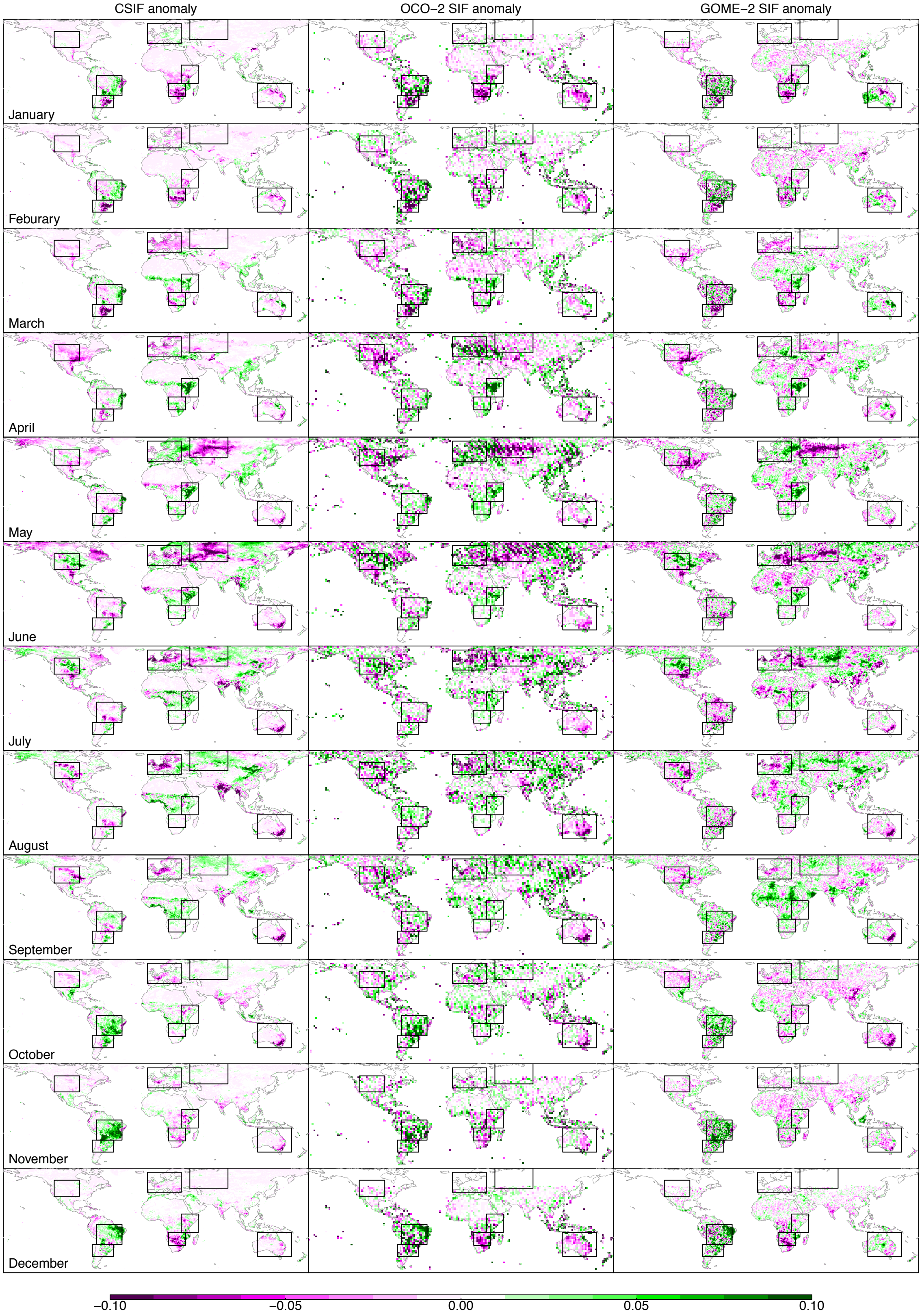

Fig. S1. Comparison between CSIF (left column), OCO-2 SIF (middle column) and GOME-2 SIF (right column) anomalies for each month in year 2018. Black boxes highlight several regions with large variability. The unit for all columns is mW m^{-2} nm^{-1} sr^{-1}. CSIF and GOME-2 SIF data are at 0.5° × 0.5° spatial resolution and OCO-2 SIF is aggregated to 2° × 2°spatial resolution due to its swath-based sampling strategy. SIF retrievals from GOME-2 is around 740nm and is converted to 757nm (CSIF and OCO-2 SIF) by dividing a factor of 1.5 (24). The sensor degradation in GOME-2 is not corrected. A 3×3 moving window average is applied for GOME-2 SIF to reduce noise. The anomaly for each month is calculated as the monthly values for 2018 minus the mean monthly values between 2014-2017.

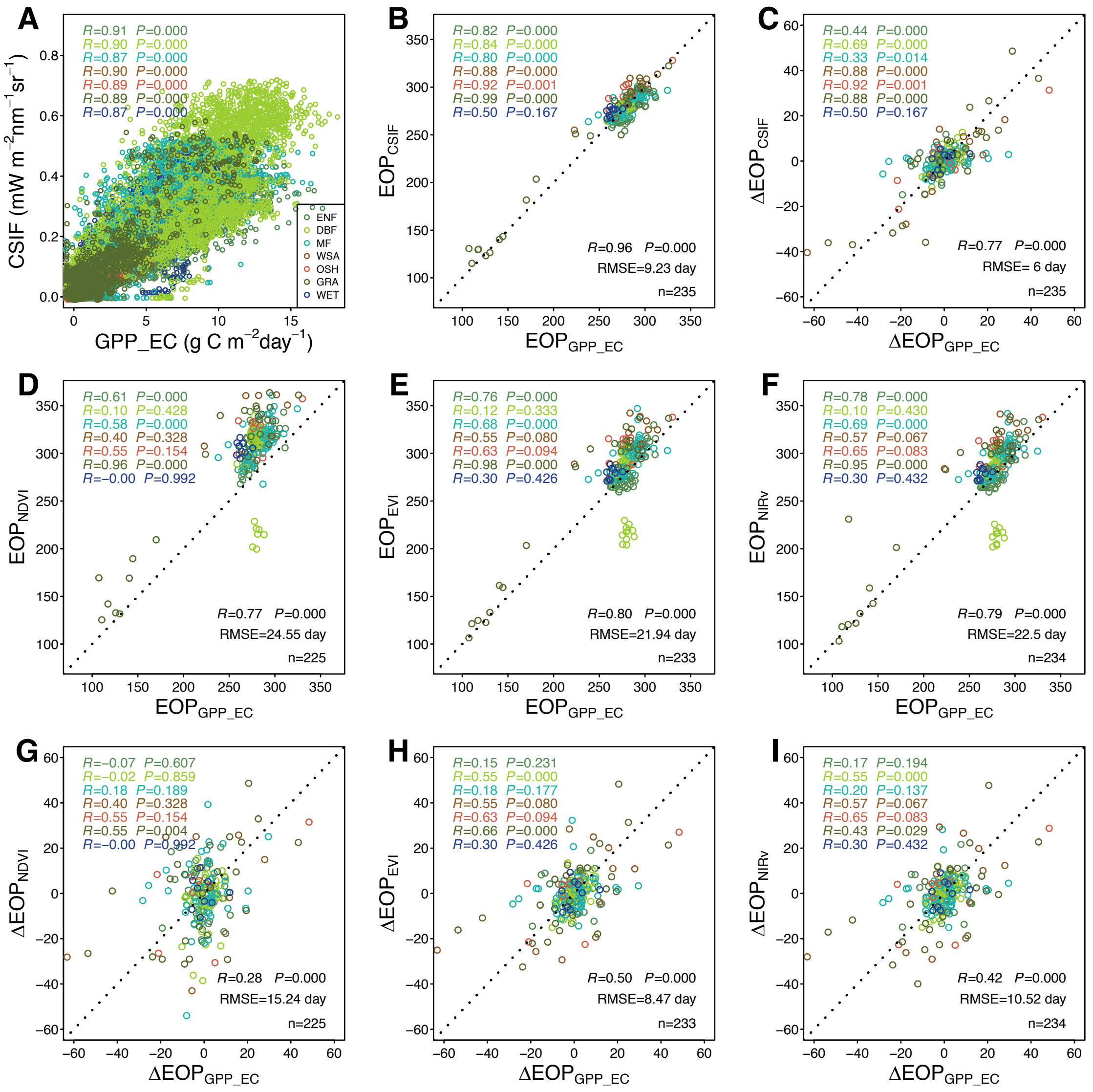

Fig. S2. Comparison between GPP with CSIF from 24 EC flux tower sites as well as other VIs. (A) Comparison between GPP and CSIF for all site-years, at 4-day temporal resolution. The correlation coefficients (*R*) and *P* values shown in the top-left corner are grouped by biome types indicated by different color (same after). (B) Comparisons of EOP derived from GPP and CSIF across all site-years. (C) Comparisons for interannual anomalies in EOP ($\Delta\mathbf{EOP}$) for each site. The anomaly is calculated as the EOP date for each year minus the multi-year average. (D-F) same as (B), but for EOP derived using NDVI, EVI and NIR_V. (G-I) same as (C), but use NDVI, EVI and NIR_V instead of CSIF. Sites used in this comparison are listed in Table S2.

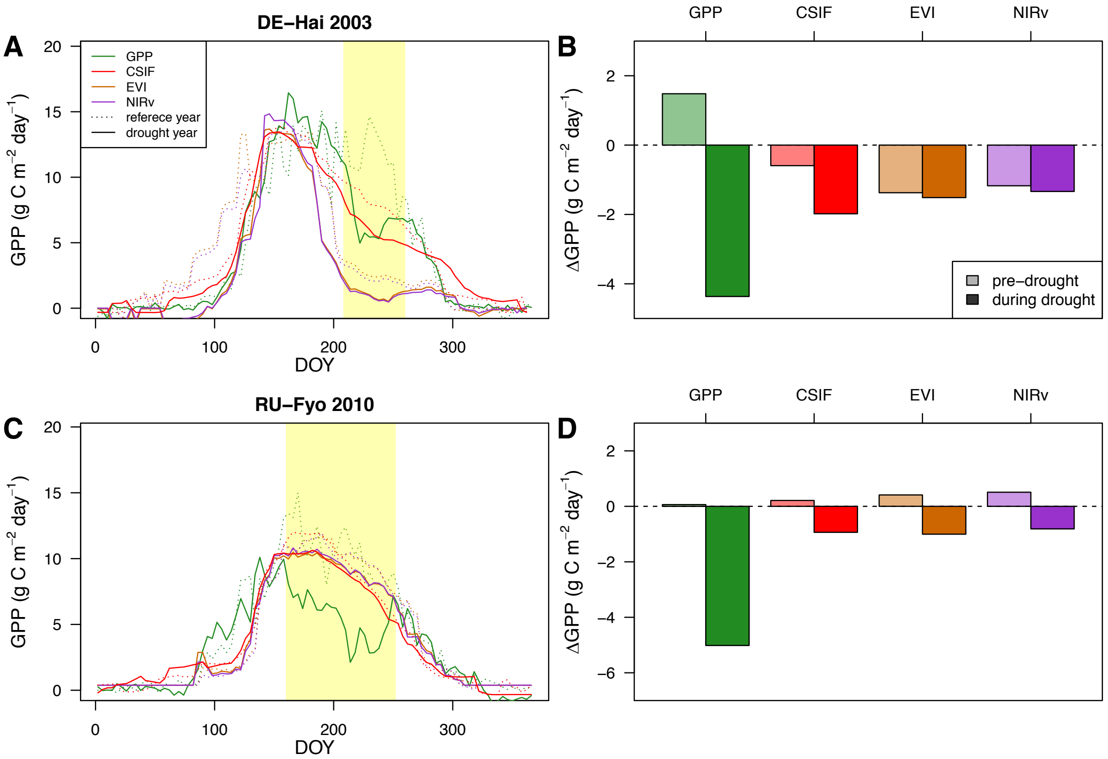

Fig. S3. Comparison of the drought sensitivity for two drought events. (A, B) Drought event for site DE-Hai (deciduous broadleaf forest in Germany) in 2003. (C, D) Drought event for site RU-Fyo (evergreen needleleaf forest in Russia) in 2010. Different colors indicate four vegetation indicators (GPP, CSIF, EVI, NIR$_V$). Dotted and solid lines in (A, C) indicate the reference year (year before drought) and drought year, respectively. Yellow shades indicate the drought period identified by GPP anomalies. Bar plots in (B and D) indicate the mean anomalies before and within the drought period. The pre drought period is defined as two months before the drought onset. For all plots, CSIF and other vegetation indicators are scaled to GPP based on their relationship with GPP using multiple year observations.

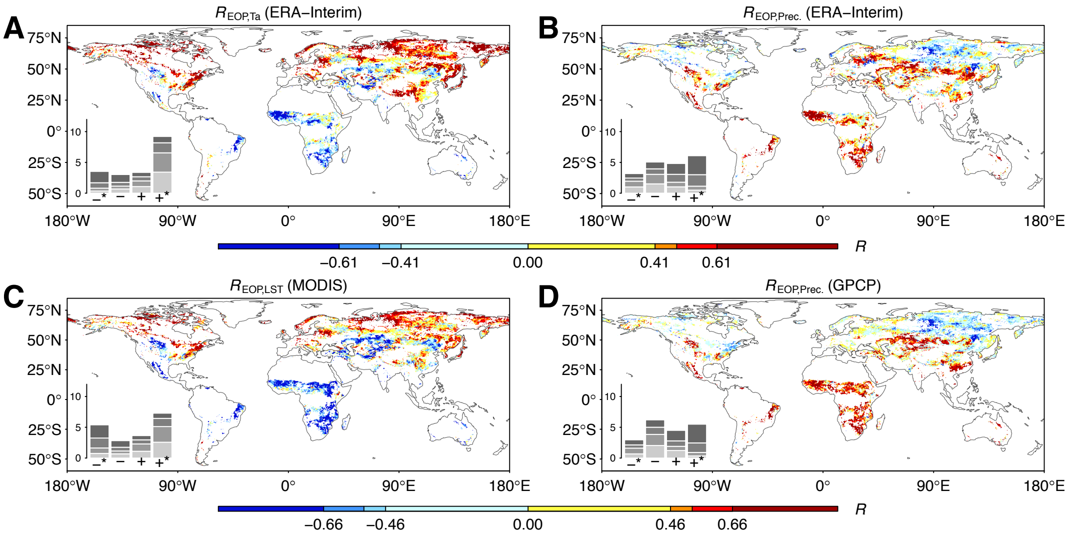

Fig. S4. Same as Fig. 1 (A-D), but using $\mathrm{NIR_V}$ instead of CSIF to retrieve physiological phenology and assess the environmental limitation.

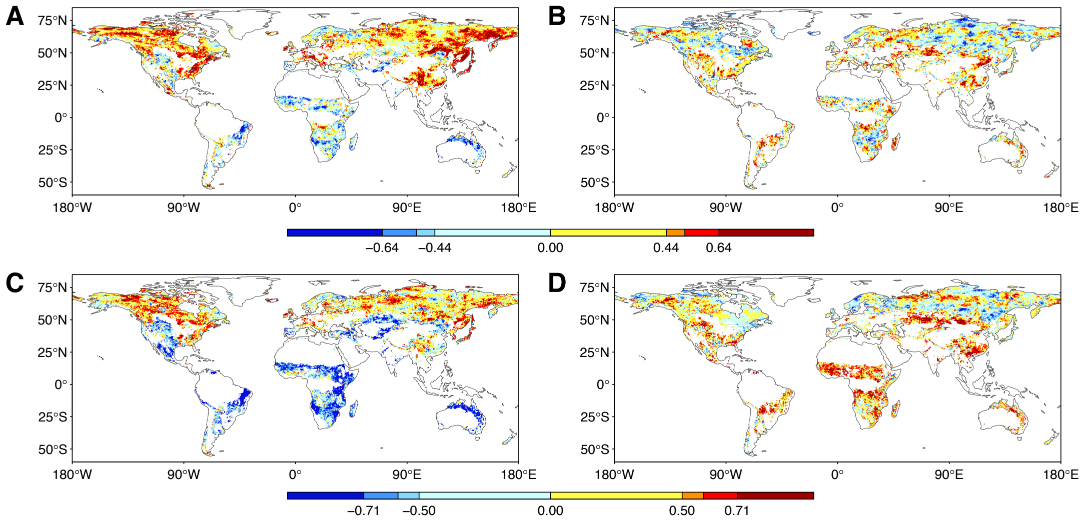

Fig. S5. Partial correlation between EOP and temperature (A,C, with precipitation and radiation controlled), or precipitation (B,D, with temperature and radiation controlled). Results are calculated with 15-day, 30-day, 60-day, and 90-day pre-season lengths and only strongest correlation were displayed for each pixel. Upper panel uses the ERA-interim dataset, lower panel uses remote sensing-based dataset (MYD13C1 for temperature, GPCP for precipitation, and BESS PAR for radiation).

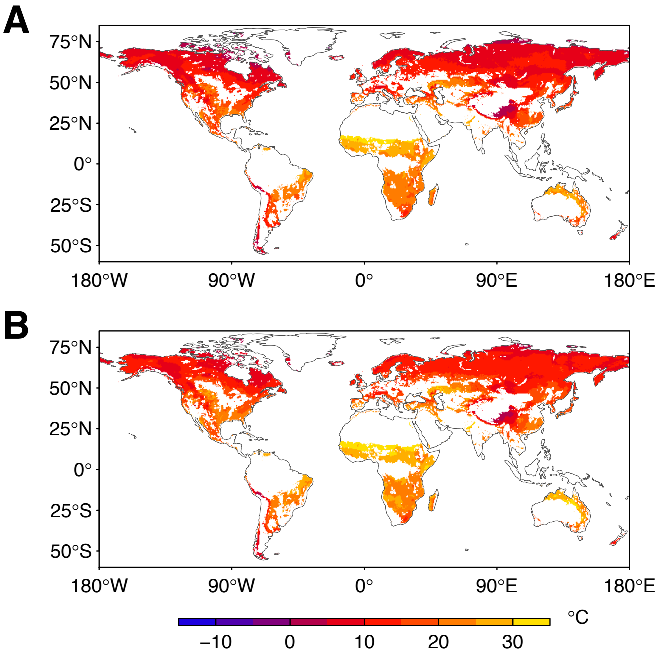

Fig. S6. Mean (A) and maximum (B) daily air temperature during 1-month pre-EOP period over 2001-2017.

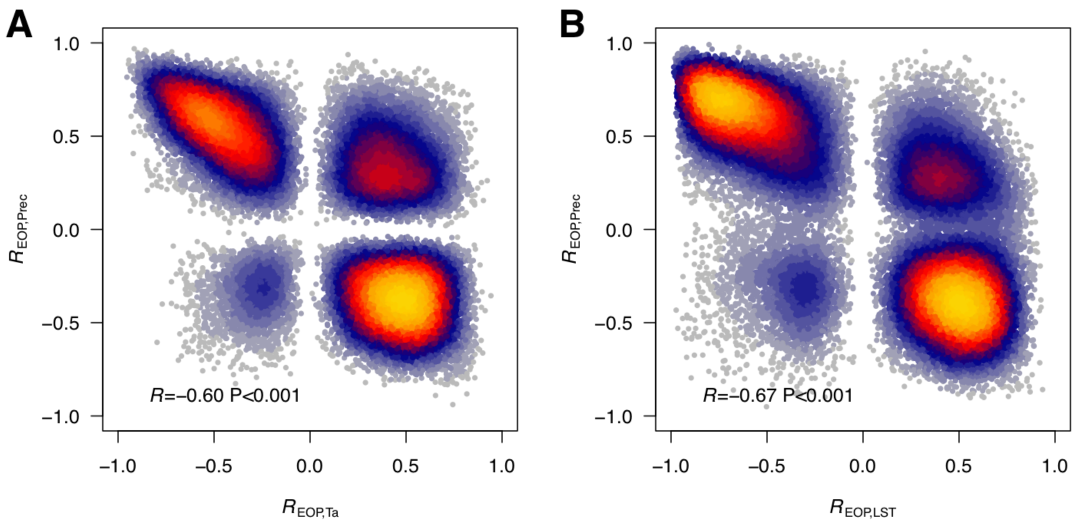

Fig. S7. Correlation between temperature-EOP correlation coefficient ($R_{EOP,Ta}$ or $R_{EOP,LST}$) and precipitation-EOP correlation coefficient ($R_{EOP,Prec}$). (A) shows the results from ERA-interim dataset, and (B) shows the remote sensing-based analysis. Warmer color indicates higher density of the points. Since the correlation coefficient for each pixel is from the strongest correlation using four different pre-season lengths, very limited pixels show close to zero *R* value.

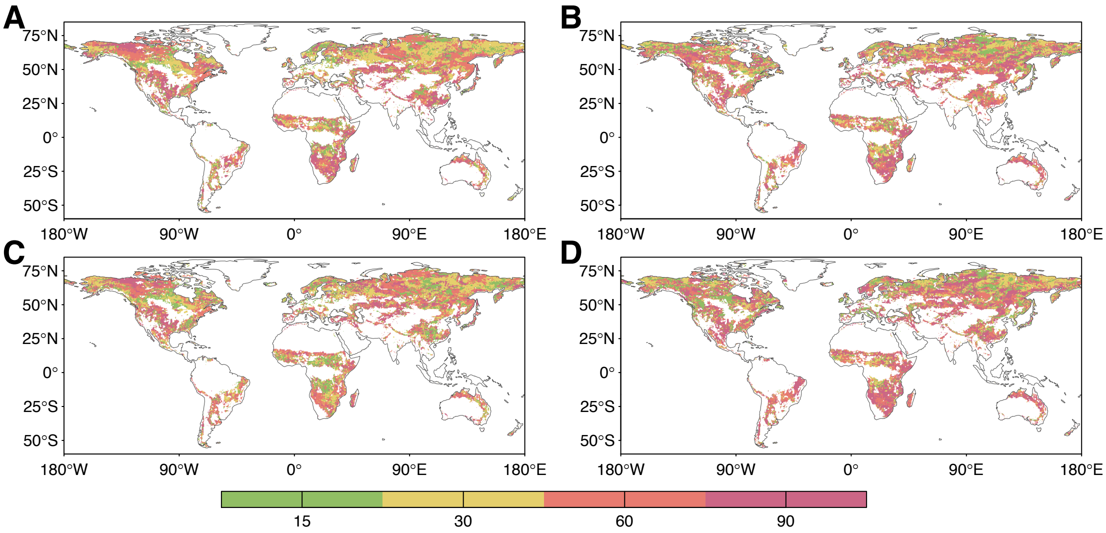

Fig. S8. Pre-season length (in days) when maximum correlation happens. (A,B) pre-season length for temperature and precipitation using ERA-Interim. (C,D) pre-season length for remote sensing based dataset.

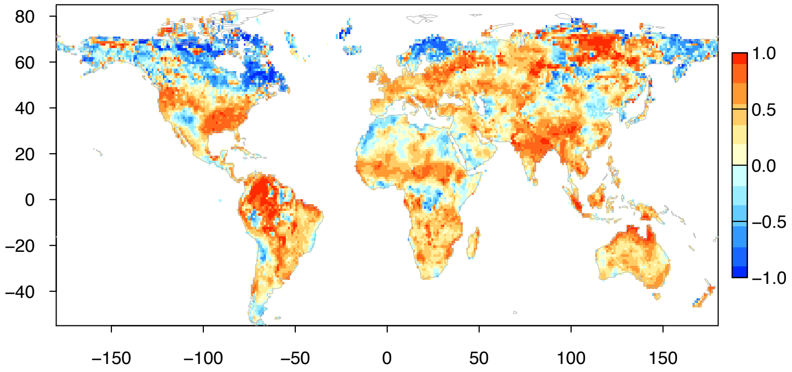

Fig. S9. Correlation coefficient for each pixel between Gravity Recovery & Climate Experiment (GRACE) liquid water equivalent thickness (LWET) and SMAP surface soil moisture (SSM). Monthly observations during the overlapping period for both datasets were used (2015-2018).

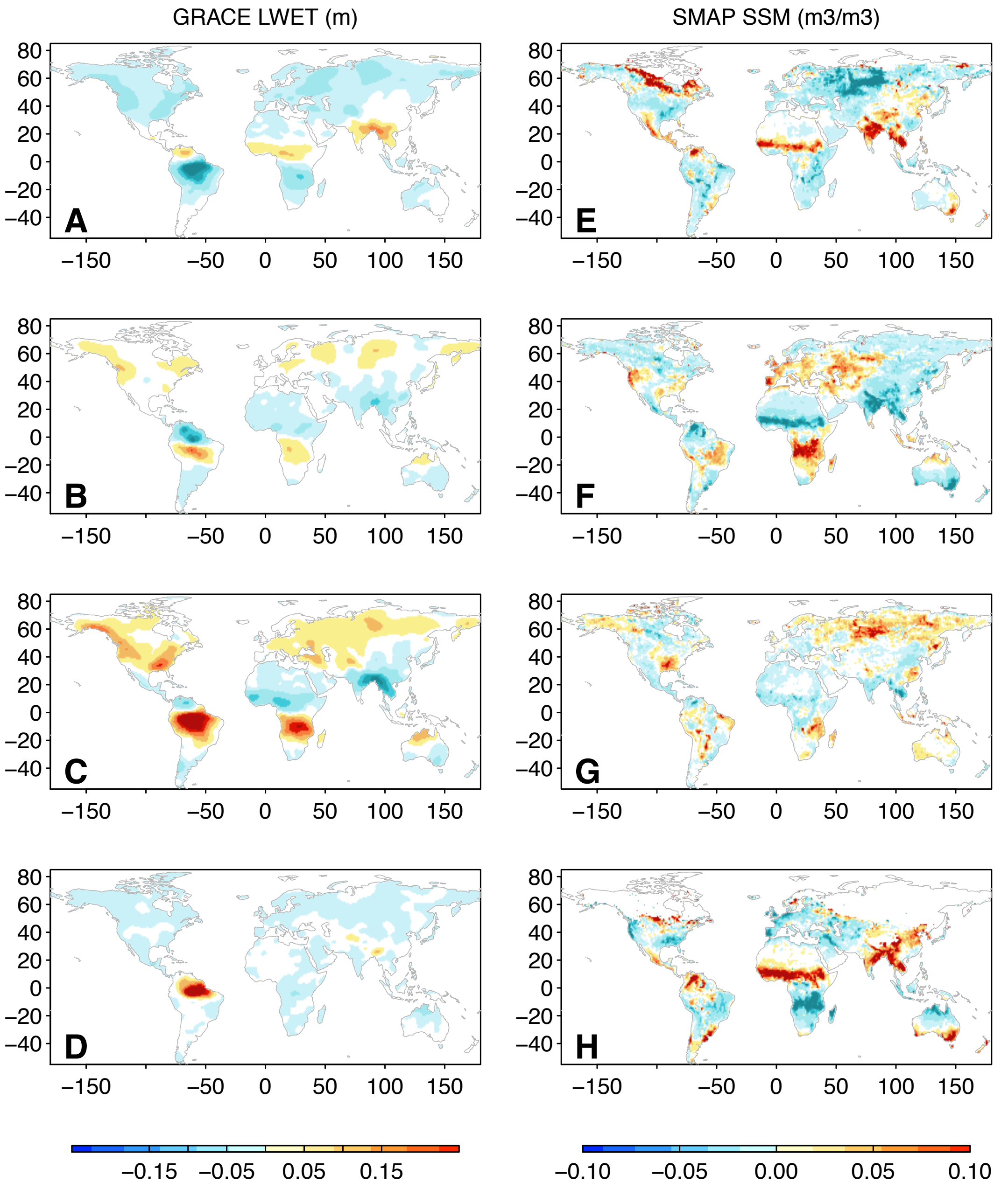

Fig. S10. Comparison of the spatial patterns of GRACE LWET anomalies (left column) and SMAP SSM anomalies (right column) for spring (A,E), summer (B,F), autumn (C,G), and winter (D,H). For each season, multi-year averages during 2015 to 2017 were used. Both GRACE LWET and SMAP SSM were also calculate as the anomaly (each season – multi-year annual mean for corresponding season) to make a fair comparison. Greenland and Antarctic were masked for clarity.

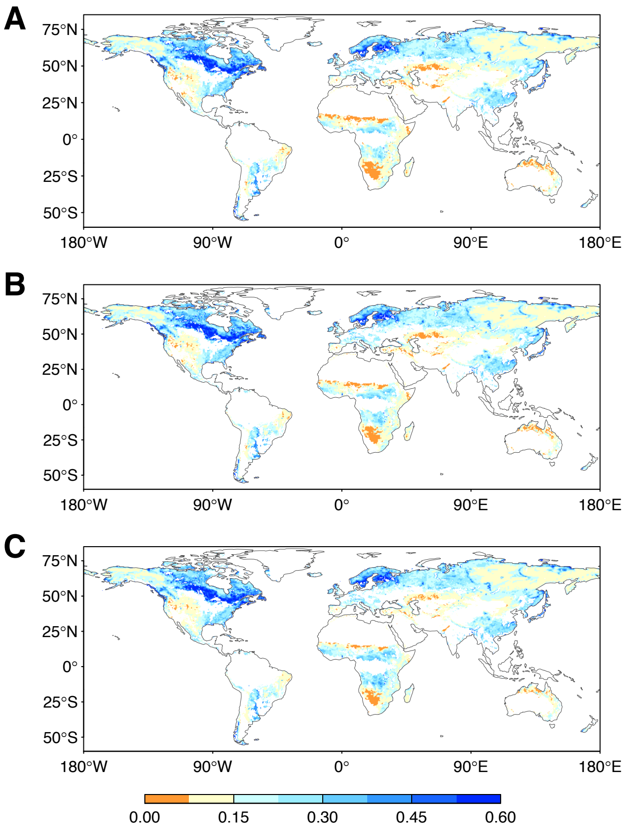

Fig. S11. Average SMAP retrieved surface soil moisture for (A) 15-day before EOP, (B) 30-day before EOP, and (C) 60-day before EOP.

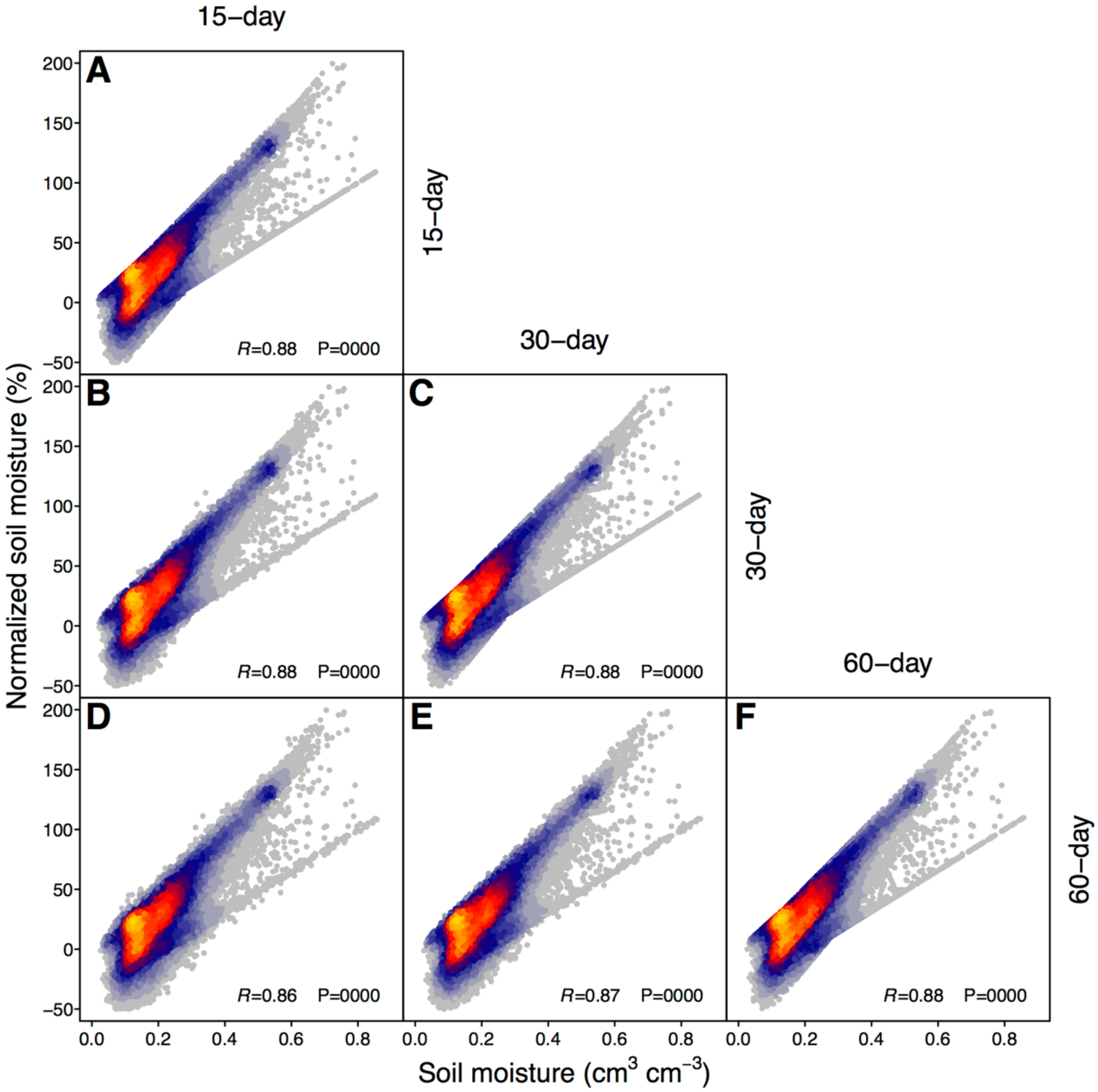

Fig. S12. Spatial correlation between the PSSM and normalized PSSM with different pre-season lengths. The PSSM is normalized by the soil porosity and wilting point as provided by the SMAP dataset (Level 4 EASE-Grid Surface and Root Zone Soil Moisture Land Model Constants (SPL4SMLM)).

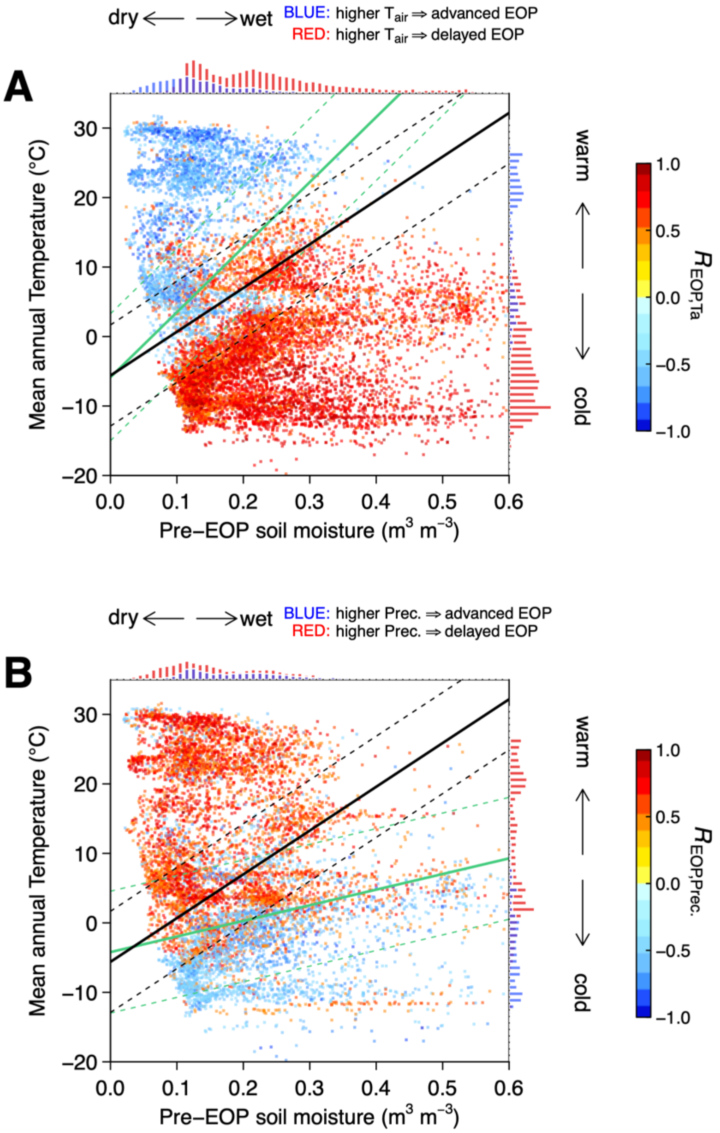

Fig. S13. Same as Fig. 2 (A, B) but using NIR_V based EOP retrievals instead of CSIF. The function for solid black line is y=62.99x-5.61.

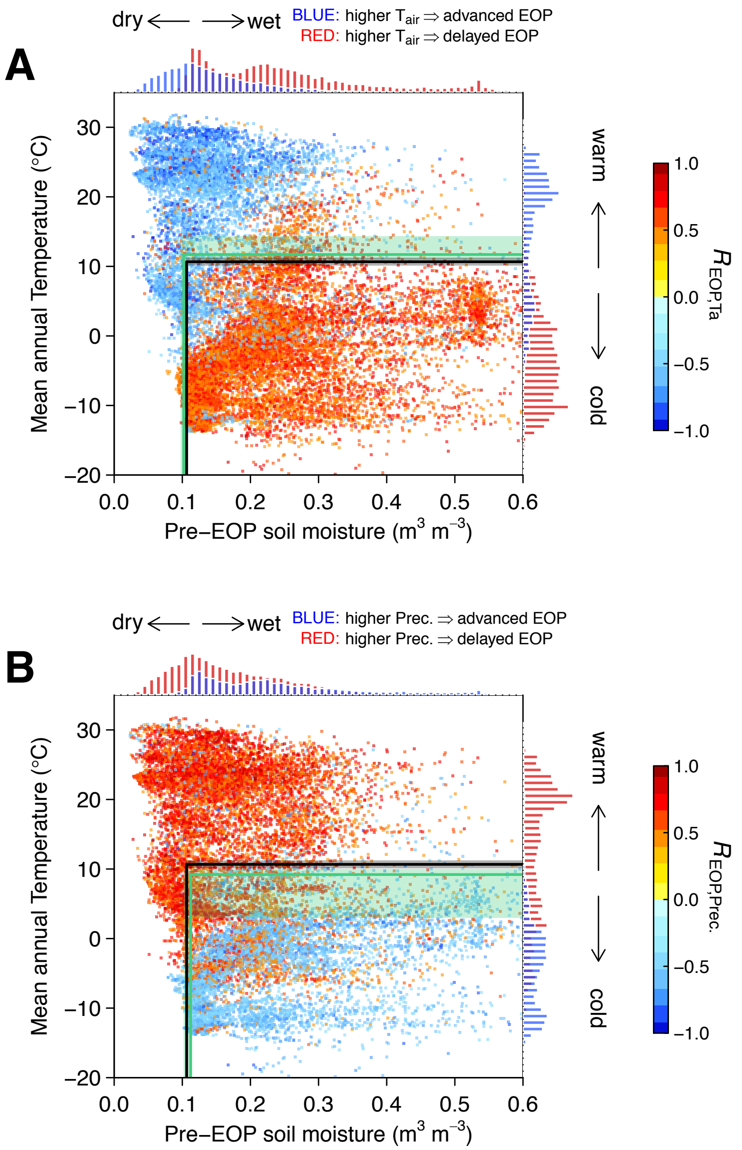

Fig. S14. Same as Fig. 2, but using the threshold-based method to separate the positive and negative correlation pixels (green), and the water and temperature limited pixels (black). The shaded area is the 5% and 95% confidence interval of the threshold generated by bootstrapping (n=2000). Solid lines indicate the median value.

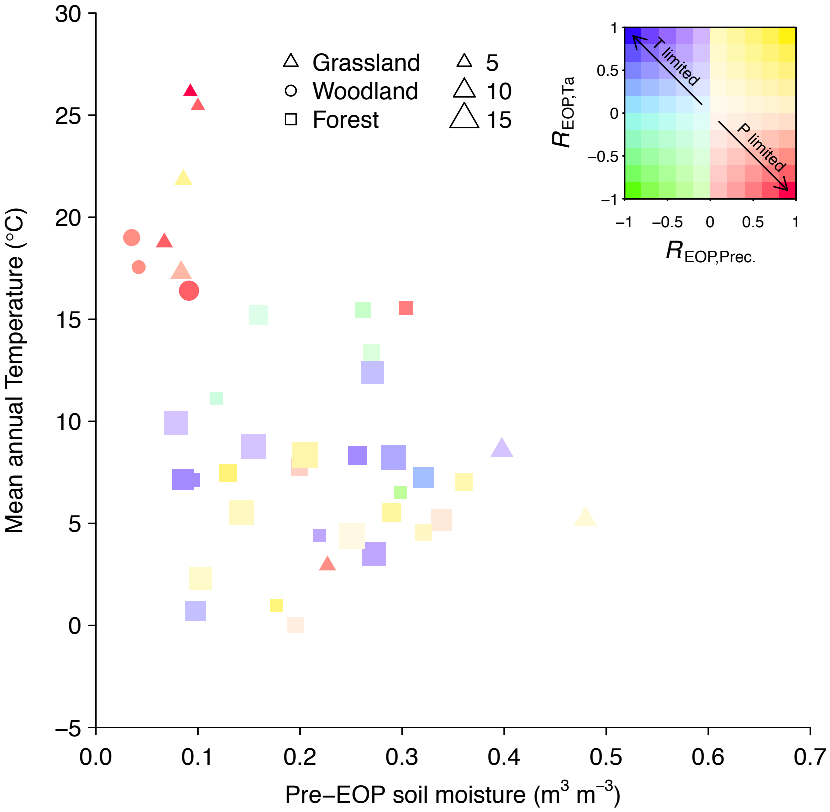

Fig. S15. Same as Figure 3, but using the *in situ* soil moisture measurement. Sites with no soil moisture measurements (n=10) was not shown in this figure.

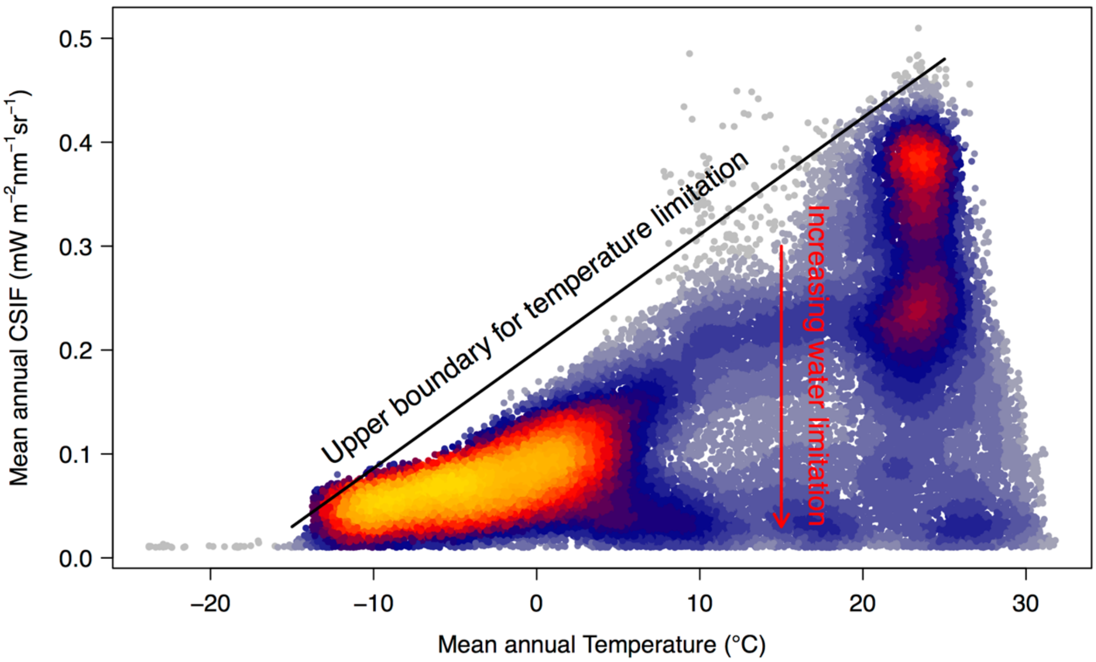

Fig. S16. Relationship between MAT and annual CSIF. Only natural vegetation (no cropland) that are not barren (mean annual CSIF>0.01 mW m^{-2} nm^{-1} sr^{-1}) were used.

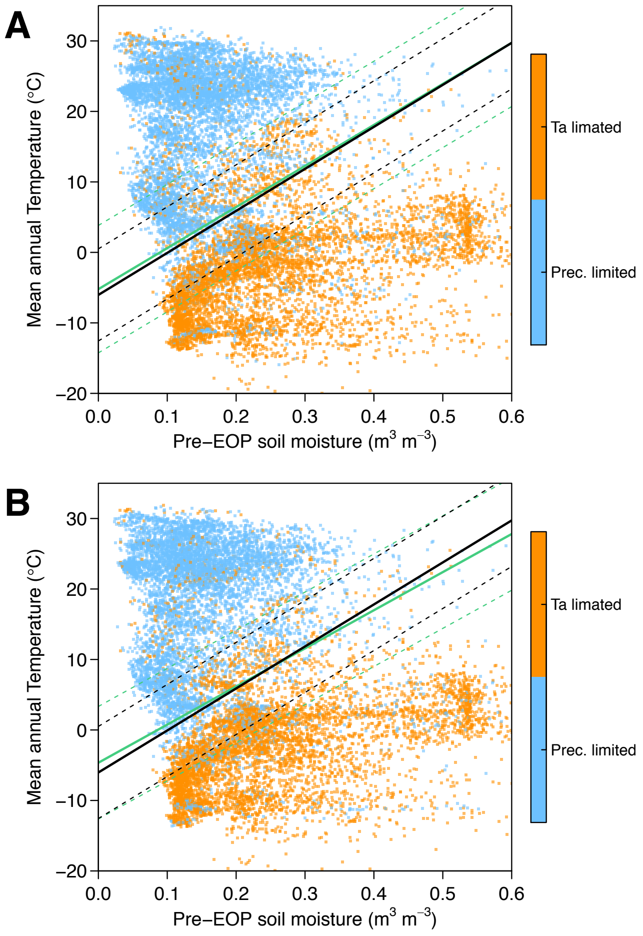

Fig. S17. Comparison between the SVM for two separate periods (A) 2001-2009 and (B) 2009-2017. The temperature and precipitation limitation, and MAT are calculated for the respective period similar to our previous analysis. While the PSSM is kept unchanged throughout time (due to data availability and limited contribution). The SVM with cyan color indicate the SVM fitted for each period, while the black lines indicate the SVM obtained from the entire study period. Kappa coefficient is 0.728 and 0.730 for 2001-2009 and 0.776 and 0.781 for 2009-2017.

.

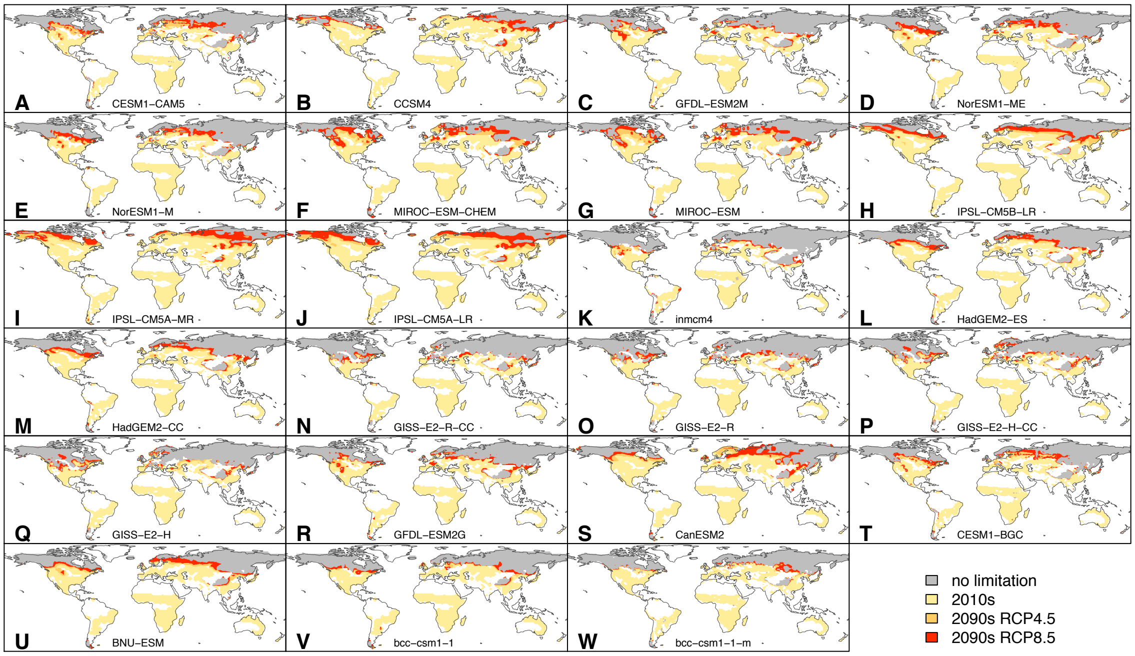

Fig. S18. Spatial patterns of changes in precipitation limited regions from each model. Yellow color represents the current extent of the water limited regions, orange and red indicate expansion of water limited regions for the end of 21st century under RCP4.5 and RCP8.5 scenarios, respectively.

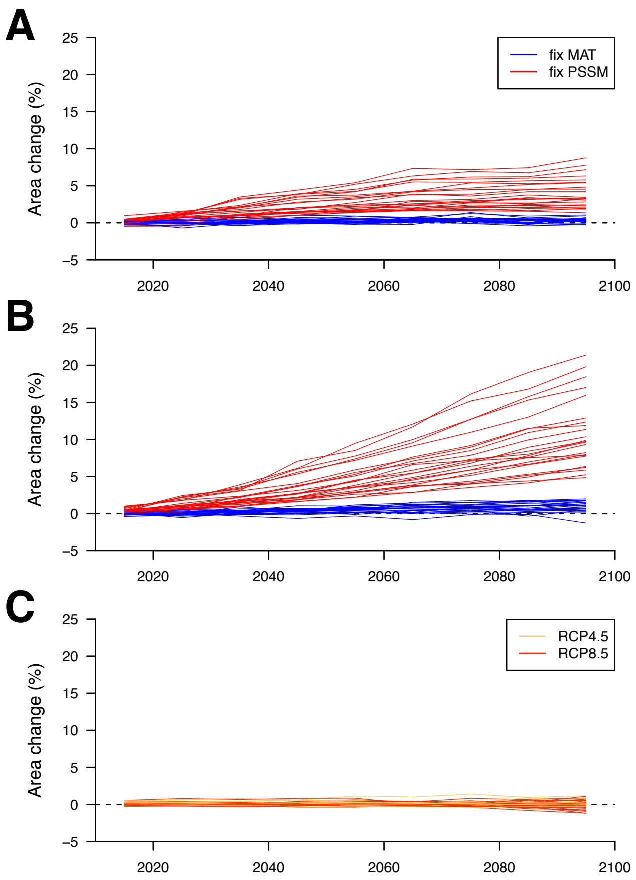

Fig. S19. Contribution of the MAT and pre-EOP SM in determining the precipitation limited regions. (A) and (B) show the areal change with using 2006-2015 as the baseline by fixing either MAT and PSSM under RCP4.5 and RCP8.5, respectively. The difference between predicted changes (considering both MAT and PSSM changes) and summation of MAT and PSSM contributions and is shown in (C).

Table S1. Comparison of classification accuracy of SVM and threshold-based algorithms (see supporting text S1).

	SVM		Threshold	
	Accuracy	Kappa	Accuracy	Kappa
Temperature	0.9064	0.7948	0.8824	0.7425
Precipitation	0.8538	0.6936	0.8013	0.5990
Temperature and precipitation	0.9125	0.8249	0.8836	0.7668

Table S2. Flux tower sites used in this study. Due to the footprint mismatch, only 24 sites are used to validate the spatial temporal and interannual variation of end of photosynthesis derived from CSIF.

Site ID	Site name	Latitude	Longitude	IGBP	Years used	CSIF validation	Ref.
AU-DaP	Daly River Savanna	-14.0633	131.3181	GRA	2008-2011, 2013	TRUE	(25)
AU-Stp	Sturt Plains	-17.1507	133.3502	GRA	2010-2014	TRUE	(25)
BE-Bra	Brasschaat	51.3092	4.5206	MF	1999-2002, 2004-2014	TRUE	(26)
BE-Vie	Vielsalm	50.3051	5.9981	MF	1997-2014	TRUE	(27)
CA-Man	Manitoba - Northern Old Black Spruce (former BOREAS Northern Study Area)	55.8796	-98.4808	ENF	1994-2003, 2008	FALSE	(28)
CA-Qfo	Quebec - Eastern Boreal, Mature Black Spruce	49.6925	-74.3421	ENF	2004-2010	TRUE	(29)
CH-Dav	Davos- Seehorn forest	46.8153	9.8559	ENF	1997-2004, 2006-2014	FALSE	(30)
CH-Lae	Laegeren	47.4781	8.365	MF	2004-2014	TRUE	(31)
CZ-wet	CZECHWET	49.0247	14.7704	WET	2006-2014	FALSE	(32)
DE-Gri	Grillenburg	50.9495	13.5125	GRA	2004-2014	FALSE	(33)
DE-Hai	Hainich	51.0792	10.453	DBF	2000-2012	TRUE	(34)
DE-Obe	Oberbärenburg	50.7836	13.7196	ENF	2008-2014	TRUE	(35)
DE-Tha	Tharandt	50.9636	13.5669	ENF	1997-2014	FALSE	(36)
DK-NuF	Nuuk Fen	64.1308	-51.3861	WET	2008-2013	FALSE	(37)
DK-Sor	Soroe	55.4859	11.6446	DBF	1996-2014	FALSE	(38)
FI-Hyy	Hyytiala	61.8475	24.295	ENF	1996-2014	TRUE	(39)
FI-Sod	Sodankyla	67.3619	26.6378	ENF	2001-2014	TRUE	(40)
FR-Fon	Fontainebleau-Barbeau	48.4764	2.7801	DBF	2005-2013	FALSE	(41)
FR-LBr	Le Bray (after 6/28/1998)	44.7171	-0.7693	ENF	1997, 2000-2008	FALSE	(42)
FR-Pue	Puechabon	43.7414	3.5958	EBF	2001-2014	FALSE	(43)
IT-Col	Collelongo- Selva Piana	41.8494	13.5881	DBF	1997-2001, 2005, 2007-2014	FALSE	(44)
IT-Lav	Lavarone	45.9562	11.2813	ENF	2003-2014	FALSE	(45)
IT-MBo	Monte Bondone	46.0147	11.0458	GRA	2003-2013	FALSE	(46)

IT-Ren	Renon	46.5869	11.4337	ENF	1999, 2002, 2003, 2005, 2007-2013	TRUE	(47)
IT-Ro1	Roccarespampani 1	42.4081	11.93	DBF	2000-2006, 2008	FALSE	(48)
IT-Ro2	Roccarespampani 2	42.3903	11.9209	DBF	2002-2007, 2010-2012	FALSE	(49)
IT-SRo	San Rossore	43.7279	10.2844	ENF	1999-2007, 2009-2012	FALSE	(50)
IT-Tor	Torgnon	45.8444	7.5781	GRA	2008-2014	FALSE	(51)
NL-Hor	Horstermeer	52.2404	5.0713	GRA	2004, 2005, 2007-2010	FALSE	(52)
NL-Loo	Loobos	52.1666	5.7436	ENF	1997-2013	FALSE	(53)
RU-Cok	Chokurdakh	70.8291	147.4943	OSH	2003-2012	FALSE	(54)
RU-Fyo	Fyodorovskoye	56.4615	32.9221	ENF	1999-2001, 2003-2014	TRUE	(55)
US-Blo	Blodgett Forest	38.8953	-120.6328	ENF	1999-2004, 2006	FALSE	(56)
US-GLE	GLEES	41.3665	-106.2399	ENF	2005-2014	FALSE	(57)
US-Ha1	Harvard Forest EMS Tower (HFR1)	42.5378	-72.1715	DBF	1992-2004, 2006, 2008-2012	TRUE	(58)
US-Los	Lost Creek	46.0827	-89.9792	WET	2001-2008, 2010, 2014	TRUE	(59)
US-Me2	Metolius-intermediate aged ponderosa pine	44.4523	-121.5574	ENF	2002, 2004-2014	FALSE	(60)
US-MMS	Morgan Monroe State Forest	39.3232	-86.4131	DBF	1999-2014	TRUE	(61)
US-NR1	Niwot Ridge Forest (LTER NWT1)	40.0329	-105.5464	ENF	1999-2014	FALSE	(62)
US-PFa	Park Falls/WLEF	45.9459	-90.2723	MF	1996-2009, 2011-2014	TRUE	(59)
US-SRG	Santa Rita Grassland	31.7894	-110.8277	GRA	2008-2014	TRUE	(63)
US-SRM	Santa Rita Mesquite	31.8214	-110.8661	WSA	2004-2014	TRUE	(64)
US-Syv	Sylvania Wilderness Area	46.242	-89.3477	MF	2002-2004, 2006, 2012-2014	TRUE	(65)
US-Ton	Tonzi Ranch	38.4316	-120.966	WSA	2001-2014	FALSE	(66)

US-UMB	Univ. of Mich. Biological Station	45.5598	-84.7138	DBF	2000-2014	TRUE	(67)
US-UMd	UMBS Disturbance	45.5625	-84.6975	DBF	2007-2014	TRUE	(68)
US-WCr	Willow Creek	45.8059	-90.0799	DBF	1999-2006, 2011-2014	TRUE	(69)
US-Whs	Walnut Gulch Lucky Hills Shrub	31.7438	-110.0522	OSH	2007-2014	TRUE	(70)
US-Wkg	Walnut Gulch Kendall Grasslands	31.7365	-109.9419	GRA	2004-2014	TRUE	(71)
ZA-Kru	Skukuza	-25.0197	31.4969	SAV	2001-2003, 2005, 2007-2010	FALSE	(72)

Table S3. CMIP5 models used in this study.

CMIP5 Models	Modeling Group	Land Component	Land Resolution	Dynamic Vegetation
bcc-csm1-1	Beijing Climate Center (BCC), China Meteorological Administration, China	BCC AVIM1.0	2.8125° × 2.8125°	Y
bcc-csm1-1-m		BCC AVIM1.0	1.125° × 1.125°	Y
BNU-ESM	College of Global Change and Earth System Science, Beijing Normal University	CoLM	2.8125° × 2.8125°	Y
CanESM2	Canadian Center for Climate Modelling and Analysis, Canada	GLASS2.7&CTEM1	2.8125° × 2.8125°	N
CCSM4	National Center for Atmospheric Research	CLM4	0.9° × 1.25°	N
CESM1-BGC	Community Earth System Model Contributors	CLM4	0.9° × 1.25°	N
CESM1-CAM5		CLM4	0.9° × 1.25°	N
GFDL-ESM2G	NOAA Geophysical Fluid Dynamics Laboratory, USA	LM3	2° × 2.5°	Y
GFDL-ESM2M		LM3	2° × 2.5°	Y
GISS-E2-H-CC	NASA Goddard Institute for Space Studies, USA	GISS-LSM-CC	2° × 2.5°	N
GISS-E2-H		GISS-LSM	2° × 2.5°	N
GISS-E2-R-CC		GISS-LSM-CC	2° × 2.5°	N
GISS-E2-R		GISS-LSM	2° × 2.5°	N
HadGEM2-CC	Met Office Hadley Centre, United Kingdom	MOSES2/TRIFFID	1.25° × 1.875	Y
HadGEM2-ES		MOSES2/TRIFFID	1.25° × 1.875°	Y
Inmcm4	Institute for Numerical Mathematics	Simple model	1.5° × 2°	N
IPSL-CM5A-LR	Institut Pierre-Simon Laplace, France	ORCHIDEE	1.875° × 3.75°	N
IPSL-CM5A-MR		ORCHIDEE	1.25° × 2.5°	N
IPSL-CM5B-LR		ORCHIDEE	1.875° × 3.75°	N
MIROC-ESM-CHEM	JAMSTEC, University of Tokyo, and NIES, Japan	MATSIRO&SEIB-DGVM	2.8125° × 2.8125°	Y
MIROC-ESM		MATSIRO&SEIB-DGVM	2.8125° × 2.8125°	Y
NorESM1-M	Norwegian Climate Centre, Norway	CLM4	1.875° × 2.5°	N
NorESM1-ME		CLM4	1.875° × 2.5°	N

References

1. Y. Zhang, J. Joiner, S. H. Alemohammad, S. Zhou, P. Gentine, A global spatially contiguous solar-induced fluorescence (CSIF) dataset using neural networks. *Biogeosciences* **15**, 5779–5800 (2018).
2. G. Tramontana, *et al.*, Predicting carbon dioxide and energy fluxes across global FLUXNET sites with regression algorithms. *Biogeosciences* **13**, 4291–4313 (2016).
3. L. Guanter, *et al.*, Retrieval and global assessment of terrestrial chlorophyll fluorescence from GOSAT space measurements. *Remote Sens. Environ.* **121**, 236–251 (2012).
4. L. Guanter, *et al.*, Global and time-resolved monitoring of crop photosynthesis with chlorophyll fluorescence. *Proc. Natl. Acad. Sci.* **111**, E1327–E1333 (2014).
5. J. Joiner, *et al.*, The seasonal cycle of satellite chlorophyll fluorescence observations and its relationship to vegetation phenology and ecosystem atmosphere carbon exchange. *Remote Sens. Environ.* **152**, 375–391 (2014).
6. K. Yang, *et al.*, Sun-induced chlorophyll fluorescence is more strongly related to absorbed light than to photosynthesis at half-hourly resolution in a rice paddy. *Remote Sens. Environ.* **216**, 658–673 (2018).
7. Y. Ryu, *et al.*, Sun-induced chlorophyll fluorescence from leaf to the globe, snap-shot to years: new lessons and opportunities in (AGU, 2019).
8. Y. Zeng, *et al.*, A practical approach for estimating the escape ratio of near-infrared solar-induced chlorophyll fluorescence. *Remote Sens. Environ.* **232**, 111209 (2019).
9. G. Badgley, C. B. Field, J. A. Berry, Canopy near-infrared reflectance and terrestrial photosynthesis. *Sci. Adv.* **3**, e1602244 (2017).
10. G. Badgley, L. D. L. Anderegg, J. A. Berry, C. B. Field, Terrestrial gross primary production: Using NIRV to scale from site to globe. *Glob. Change Biol.* **25**, 3731–3740 (2019).
11. J. R. Ehleringer, J. Comstock, Leaf absorptance and leaf angle: mechanisms for stress avoidance in *Plant Response to Stress*, NATO ASI Series., J. D. Tenhunen, F. M. Catarino, O. L. Lange, W. C. Oechel, Eds. (Springer, 1987), pp. 55–76.
12. B. Dechant, *et al.*, Canopy structure explains the relationship between photosynthesis and sun-induced chlorophyll fluorescence in crops. *EarthArXiv* (2019) https:/doi.org/10.31223/osf.io/cbxpq (October 30, 2019).
13. T. S. Magney, *et al.*, Mechanistic evidence for tracking the seasonality of photosynthesis with solar-induced fluorescence. *Proc. Natl. Acad. Sci.*, 201900278 (2019).
14. B. D. Stocker, *et al.*, Drought impacts on terrestrial primary production underestimated by satellite monitoring. *Nat. Geosci.*, 1 (2019).
15. Q. Liu, *et al.*, Delayed autumn phenology in the Northern Hemisphere is related to change in both climate and spring phenology. *Glob. Change Biol.* **22**, 3702–3711 (2016).
16. P. Berrisford, *et al.*, “The ERA-Interim archive, version 2.0” (ECMWF, 2011) (March 22, 2019).
17. K. Gallo, R. Hale, D. Tarpley, Y. Yu, Evaluation of the Relationship between Air and Land Surface Temperature under Clear- and Cloudy-Sky Conditions. *J. Appl. Meteorol. Climatol.* **50**, 767–775 (2010).
18. G. J. Huffman, *et al.*, The Global Precipitation Climatology Project (GPCP)

Combined Precipitation Dataset. *Bull. Am. Meteorol. Soc.* **78**, 5–20 (1997).
19. G. J. Huffman, *et al.*, Global Precipitation at One-Degree Daily Resolution from Multisatellite Observations. *J. Hydrometeorol.* **2**, 36–50 (2001).
20. Y. Ryu, C. Jiang, H. Kobayashi, M. Detto, MODIS-derived global land products of shortwave radiation and diffuse and total photosynthetically active radiation at 5km resolution from 2000. *Remote Sens. Environ.* **204**, 812–825 (2018).
21. D. Entekhabi, *et al.*, SMAP Handbook–Soil Moisture Active Passive: Mapping Soil Moisture and Freeze/Thaw from Space (2014) (March 20, 2019).
22. W. Dorigo, *et al.*, ESA CCI Soil Moisture for improved Earth system understanding: State-of-the art and future directions. *Remote Sens. Environ.* **203**, 185–215 (2017).
23. M. Reichstein, *et al.*, On the separation of net ecosystem exchange into assimilation and ecosystem respiration: Review and improved algorithm. *Glob. Change Biol.* **11**, 1424–1439 (2005).
24. N. C. Parazoo, *et al.*, Towards a Harmonized Long-Term Spaceborne Record of Far-Red Solar-Induced Fluorescence. *J. Geophys. Res. Biogeosciences* **124**, 2518–2539 (2019).
25. J. Beringer, L. B. Hutley, J. M. Hacker, B. Neininger, K. T. Paw U, Patterns and processes of carbon, water and energy cycles across northern Australian landscapes: From point to region. *Agric. For. Meteorol.* **151**, 1409–1416 (2011).
26. I. A. Janssens, A. S. Kowalski, R. Ceulemans, Forest floor CO 2 fluxes estimated by eddy covariance and chamber-based model. *Agric. For. Meteorol.* **106**, 61–69 (2001).
27. M. Aubinet, *et al.*, Long term carbon dioxide exchange above a mixed forest in the Belgian Ardennes. *Agric. For. Meteorol.* **108**, 293–315 (2001).
28. C. Wang, B. Bond-Lamberty, S. T. Gower, Carbon distribution of a well- and poorly-drained black spruce fire chronosequence. *Glob. Change Biol.* **9**, 1066–1079 (2003).
29. O. Bergeron, *et al.*, Comparison of carbon dioxide fluxes over three boreal black spruce forests in Canada. *Glob. Change Biol.* **13**, 89–107 (2006).
30. S. Zielis, *et al.*, NEP of a Swiss subalpine forest is significantly driven not only by current but also by previous year's weather. *Biogeosciences* **11**, 1627–1635 (2014).
31. M. Göckede, *et al.*, Quality control of CarboEurope flux data – Part 1: Coupling footprint analyses with flux data quality assessment to evaluate sites in forest ecosystems. *Biogeosciences* **5**, 433–450 (2008).
32. J. Dušek, H. Čížková, S. Stellner, R. Czerný, J. Květ, Fluctuating water table affects gross ecosystem production and gross radiation use efficiency in a sedge-grass marsh. *Hydrobiologia* **692**, 57–66 (2012).
33. A.-K. Prescher, T. Grünwald, C. Bernhofer, Land use regulates carbon budgets in eastern Germany: From NEE to NBP. *Agric. For. Meteorol.* **150**, 1016–1025 (2010).
34. P. M. Anthoni, *et al.*, Forest and agricultural land-use-dependent CO2 exchange in Thuringia, Germany. *Glob. Change Biol.* **10**, 2005–2019 (2004).
35. C. Bernhofer, *et al.*, (2008-2014) FLUXNET2015 DE-Obe Oberbärenburg, 10.18140/FLX/1440151.
36. T. Grünwald, C. Bernhofer, A decade of carbon, water and energy flux measurements of an old spruce forest at the Anchor Station Tharandt. *Tellus B* **59**, 387–396 (2007).

37. A. Westergaard-Nielsen, M. Lund, B. U. Hansen, M. P. Tamstorf, Camera derived vegetation greenness index as proxy for gross primary production in a low Arctic wetland area. *ISPRS J. Photogramm. Remote Sens.* **86**, 89–99 (2013).
38. K. Pilegaard, A. Ibrom, M. S. Courtney, P. Hummelshøj, N. O. Jensen, Increasing net CO2 uptake by a Danish beech forest during the period from 1996 to 2009. *Agric. For. Meteorol.* **151**, 934–946 (2011).
39. T. Vesala, *et al.*, Effect of thinning on surface fluxes in a boreal forest. *Glob. Biogeochem. Cycles* **19** (2005).
40. T. Suni, *et al.*, Long-term measurements of surface fluxes above a Scots pine forest in Hyytiala, southern Finland, 1996-2001. *Boreal Environ. Res.* **8**, 287–302 (2003).
41. N. Delpierre, D. Berveiller, E. Granda, E. Dufrêne, Wood phenology, not carbon input, controls the interannual variability of wood growth in a temperate oak forest. *New Phytol.* **210**, 459–470 (2016).
42. P. Berbigier, J.-M. Bonnefond, P. Mellmann, CO2 and water vapour fluxes for 2 years above Euroflux forest site. *Agric. For. Meteorol.* **108**, 183–197 (2001).
43. S. Rambal, R. Joffre, J. M. Ourcival, J. Cavender-Bares, A. Rocheteau, The growth respiration component in eddy CO2 flux from a Quercus ilex mediterranean forest. *Glob. Change Biol.* **10**, 1460–1469 (2004).
44. R. Valentini, *et al.*, Seasonal net carbon dioxide exchange of a beech forest with the atmosphere. *Glob. Change Biol.* **2**, 199–207 (1996).
45. B. Marcolla, A. Pitacco, A. Cescatti, Canopy Architecture and Turbulence Structure in a Coniferous Forest. *Bound.-Layer Meteorol.* **108**, 39–59 (2003).
46. B. Marcolla, *et al.*, Climatic controls and ecosystem responses drive the inter-annual variability of the net ecosystem exchange of an alpine meadow. *Agric. For. Meteorol.* **151**, 1233–1243 (2011).
47. B. Marcolla, *et al.*, Importance of advection in the atmospheric CO2 exchanges of an alpine forest. *Agric. For. Meteorol.* **130**, 193–206 (2005).
48. A. Rey, *et al.*, Annual variation in soil respiration and its components in a coppice oak forest in Central Italy. *Glob. Change Biol.* **8**, 851–866 (2002).
49. V. Tedeschi, *et al.*, Soil respiration in a Mediterranean oak forest at different developmental stages after coppicing. *Glob. Change Biol.* **12**, 110–121 (2006).
50. M. Chiesi, *et al.*, Modelling carbon budget of Mediterranean forests using ground and remote sensing measurements. *Agric. For. Meteorol.* **135**, 22–34 (2005).
51. M. Galvagno, *et al.*, Phenology and carbon dioxide source/sink strength of a subalpine grassland in response to an exceptionally short snow season. *Environ. Res. Lett.* **8**, 025008 (2013).
52. C. M. J. Jacobs, *et al.*, Variability of annual CO_2 exchange from Dutch grasslands. *Biogeosciences* **4**, 803–816 (2007).
53. A. J. Dolman, E. J. Moors, J. A. Elbers, The carbon uptake of a mid latitude pine forest growing on sandy soil. *Agric. For. Meteorol.* **111**, 157–170 (2002).
54. M. K. van der Molen, *et al.*, The growing season greenhouse gas balance of a continental tundra site in the Indigirka lowlands, NE Siberia. *Biogeosciences* **4**, 985–1003 (2007).
55. J. Kurbatova, C. Li, A. Varlagin, X. Xiao, N. Vygodskaya, Modeling carbon dynamics in two adjacent spruce forests with different soil conditions in Russia. *Biogeosciences* **5**, 969–980 (2008).

56. B. N. Sulman, A. R. Desai, B. D. Cook, N. Saliendra, D. S. Mackay, Contrasting carbon dioxide fluxes between a drying shrub wetland in Northern Wisconsin, USA, and nearby forests. *Biogeosciences* **6**, 1115–1126 (2009).
57. J. M. Frank, W. J. Massman, B. E. Ewers, L. S. Huckaby, J. F. Negrón, Ecosystem CO2/H2O fluxes are explained by hydraulically limited gas exchange during tree mortality from spruce bark beetles. *J. Geophys. Res. Biogeosciences* **119**, 1195–1215 (2014).
58. C. C. Barford, Factors Controlling Long- and Short-Term Sequestration of Atmospheric CO2 in a Mid-latitude Forest. *Science* **294**, 1688–1691 (2001).
59. A. R. Desai, *et al.*, Landscape-level terrestrial methane flux observed from a very tall tower. *Agric. For. Meteorol.* **201**, 61–75 (2015).
60. J. L. Campbell, O. J. Sun, B. E. Law, Disturbance and net ecosystem production across three climatically distinct forest landscapes. *Glob. Biogeochem. Cycles* **18** (2004).
61. H. P. Schmid, C. S. B. Grimmond, F. Cropley, B. Offerle, H.-B. Su, Measurements of CO2 and energy fluxes over a mixed hardwood forest in the mid-western United States. *Agric. For. Meteorol.* **103**, 357–374 (2000).
62. R. K. Monson, *et al.*, Carbon sequestration in a high-elevation, subalpine forest. *Glob. Change Biol.* **8**, 459–478 (2002).
63. R. L. Scott, J. A. Biederman, E. P. Hamerlynck, G. A. Barron-Gafford, The carbon balance pivot point of southwestern U.S. semiarid ecosystems: Insights from the 21st century drought. *J. Geophys. Res. G Biogeosciences* **120**, 2612–2624 (2015).
64. R. L. Scott, G. D. Jenerette, D. L. Potts, T. E. Huxman, Effects of seasonal drought on net carbon dioxide exchange from a woody-plant-encroached semiarid grassland. *J. Geophys. Res. Biogeosciences* **114** (2009).
65. A. R. Desai, P. V. Bolstad, B. D. Cook, K. J. Davis, E. V. Carey, Comparing net ecosystem exchange of carbon dioxide between an old-growth and mature forest in the upper Midwest, USA. *Agric. For. Meteorol.* **128**, 33–55 (2005).
66. D. D. Baldocchi, L. Xu, N. Kiang, How plant functional-type, weather, seasonal drought, and soil physical properties alter water and energy fluxes of an oak–grass savanna and an annual grassland. *Agric. For. Meteorol.* **123**, 13–39 (2004).
67. C. M. Gough, *et al.*, Sustained carbon uptake and storage following moderate disturbance in a Great Lakes forest. *Ecol. Appl.* **23**, 1202–1215 (2013).
68. L. E. Nave, *et al.*, Disturbance and the resilience of coupled carbon and nitrogen cycling in a north temperate forest. *J. Geophys. Res. Biogeosciences* **116** (2011).
69. B. D. Cook, *et al.*, Carbon exchange and venting anomalies in an upland deciduous forest in northern Wisconsin, USA. *Agric. For. Meteorol.* **126**, 271–295 (2004).
70. R. L. Scott, T. E. Huxman, W. L. Cable, W. E. Emmerich, Partitioning of evapotranspiration and its relation to carbon dioxide exchange in a Chihuahuan Desert shrubland. *Hydrol. Process.* **20**, 3227–3243 (2006).
71. R. L. Scott, E. P. Hamerlynck, G. D. Jenerette, M. S. Moran, G. A. Barron-Gafford, Carbon dioxide exchange in a semidesert grassland through drought-induced vegetation change. *J. Geophys. Res. Biogeosciences* **115**, 1–12 (2010).
72. S. A. Archibald, *et al.*, Drivers of inter-annual variability in Net Ecosystem Exchange in a semi-arid savanna ecosystem, South Africa. *Biogeosciences* **6**, 251–266 (2009).